# Cross sections for the exclusive photon electroproduction on the proton and Generalized Parton Distributions

H.S. Jo,[1, *] F.X. Girod,[2, 3] H. Avakian,[2] V.D. Burkert,[2] M. Garçon,[3] M. Guidal,[1] V. Kubarovsky,[2, 4] S. Niccolai,[1]
P. Stoler,[4] K.P. Adhikari,[28] D. Adikaram,[28, †] M.J. Amaryan,[28] M.D. Anderson,[36] S. Anefalos Pereira,[18]
J. Ball,[3] N.A. Baltzell,[5, 32] M. Battaglieri,[19] V. Batourine,[2, 24] I. Bedlinskiy,[22] A.S. Biselli,[12] S. Boiarinov,[2]
W.J. Briscoe,[15] W.K. Brooks,[34, 2] D.S. Carman,[2] A. Celentano,[19] S. Chandavar,[27] G. Charles,[1] L. Colaneri,[20, 30]
P.L. Cole,[16] N. Compton,[27] M. Contalbrigo,[17] V. Crede,[14] A. D'Angelo,[20, 30] N. Dashyan,[40] R. De Vita,[19]
E. De Sanctis,[18] A. Deur,[2] C. Djalali,[32] R. Dupre,[1] A. El Alaoui,[34] L. El Fassi,[28, ‡] L. Elouadrhiri,[2] G. Fedotov,[32, 31]
S. Fegan,[19] A. Filippi,[21] J.A. Fleming,[35] B. Garillon,[1] N. Gevorgyan,[40] Y. Ghandilyan,[40] G.P. Gilfoyle,[29]
K.L. Giovanetti,[23] J.T. Goetz,[27] E. Golovatch,[31] R.W. Gothe,[32] K.A. Griffioen,[39] B. Guegan,[1] N. Guler,[28, §]
L. Guo,[13, 2] K. Hafidi,[5] H. Hakobyan,[34, 40] N. Harrison,[11] M. Hattawy,[1] K. Hicks,[27] N. Hirlinger Saylor,[4]
D. Ho,[9] M. Holtrop,[25] S.M. Hughes,[35] Y. Ilieva,[32, 15] D.G. Ireland,[36] B.S. Ishkhanov,[31] D. Jenkins,[37] K. Joo,[11]
S. Joosten,[33] D. Keller,[38] G. Khachatryan,[40] M. Khandaker,[16, 26] A. Kim,[11] W. Kim,[24] A. Klein,[28] F.J. Klein,[10]
S.E. Kuhn,[28] S.V. Kuleshov,[34, 22] P. Lenisa,[17] K. Livingston,[36] H.Y. Lu,[32] I.J.D. MacGregor,[36] B. McKinnon,[36]
Z.E. Meziani,[33] M. Mirazita,[18] V. Mokeev,[2, 31] R.A. Montgomery,[18] H. Moutarde,[3] A Movsisyan,[17] E. Munevar,[2]
C. Munoz Camacho,[1] P. Nadel-Turonski,[2, 15] L.A. Net,[32] G. Niculescu,[23] M. Osipenko,[19] A.I. Ostrovidov,[14]
M. Paolone,[33] K. Park,[2, 24, ¶] E. Pasyuk,[2] J.J. Phillips,[36] S. Pisano,[18] O. Pogorelko,[22] J.W. Price,[7] S. Procureur,[3]
Y. Prok,[28, 2] A.J.R. Puckett,[11] B.A. Raue,[13, 2] M. Ripani,[19] A. Rizzo,[20, 30] G. Rosner,[36] P. Rossi,[2, 18] P. Roy,[14]
F. Sabatié,[3] C. Salgado,[26] D. Schott,[15] R.A. Schumacher,[9] E. Seder,[11] A. Simonyan,[40] Iu. Skorodumina,[32, 31]
G.D. Smith,[35] D. Sokhan,[36] N. Sparveris,[33] S. Stepanyan,[2] I.I. Strakovsky,[15] S. Strauch,[32] V. Sytnik,[34] Ye Tian,[32]
S. Tkachenko,[38] M. Ungaro,[2, 11] H. Voskanyan,[40] E. Voutier,[1] N.K. Walford,[10] D.P. Watts,[35] X. Wei,[2]
L.B. Weinstein,[28] M.H. Wood,[8, 32] N. Zachariou,[32] L. Zana,[35, 25] J. Zhang,[2, 28] Z.W. Zhao,[28, 2] and I. Zonta[20, 30]

(The CLAS Collaboration)

[1] *Institut de Physique Nucléaire, CNRS/IN2P3 and Université Paris Sud, Orsay, France*
[2] *Thomas Jefferson National Accelerator Facility, Newport News, Virginia 23606*
[3] *CEA, Centre de Saclay, Irfu/Service de Physique Nucléaire, 91191 Gif-sur-Yvette, France*
[4] *Rensselaer Polytechnic Institute, Troy, New York 12180-3590*
[5] *Argonne National Laboratory, Argonne, Illinois 60439*
[6] *Arizona State University, Tempe, Arizona 85287-1504*
[7] *California State University, Dominguez Hills, Carson, CA 90747*
[8] *Canisius College, Buffalo, NY*
[9] *Carnegie Mellon University, Pittsburgh, Pennsylvania 15213*
[10] *Catholic University of America, Washington, D.C. 20064*
[11] *University of Connecticut, Storrs, Connecticut 06269*
[12] *Fairfield University, Fairfield CT 06824*
[13] *Florida International University, Miami, Florida 33199*
[14] *Florida State University, Tallahassee, Florida 32306*
[15] *The George Washington University, Washington, DC 20052*
[16] *Idaho State University, Pocatello, Idaho 83209*
[17] *INFN, Sezione di Ferrara, 44100 Ferrara, Italy*
[18] *INFN, Laboratori Nazionali di Frascati, 00044 Frascati, Italy*
[19] *INFN, Sezione di Genova, 16146 Genova, Italy*
[20] *INFN, Sezione di Roma Tor Vergata, 00133 Rome, Italy*
[21] *INFN, Sezione di Torino, 10125 Torino, Italy*
[22] *Institute of Theoretical and Experimental Physics, Moscow, 117259, Russia*
[23] *James Madison University, Harrisonburg, Virginia 22807*
[24] *Kyungpook National University, Daegu 702-701, Republic of Korea*
[25] *University of New Hampshire, Durham, New Hampshire 03824-3568*
[26] *Norfolk State University, Norfolk, Virginia 23504*
[27] *Ohio University, Athens, Ohio 45701*
[28] *Old Dominion University, Norfolk, Virginia 23529*
[29] *University of Richmond, Richmond, Virginia 23173*
[30] *Universita' di Roma Tor Vergata, 00133 Rome Italy*
[31] *Skobeltsyn Institute of Nuclear Physics, Lomonosov Moscow State University, 119234 Moscow, Russia*
[32] *University of South Carolina, Columbia, South Carolina 29208*
[33] *Temple University, Philadelphia, PA 19122*
[34] *Universidad Técnica Federico Santa María, Casilla 110-V Valparaíso, Chile*

[35] *Edinburgh University, Edinburgh EH9 3JZ, United Kingdom*
[36] *University of Glasgow, Glasgow G12 8QQ, United Kingdom*
[37] *Virginia Tech, Blacksburg, Virginia 24061-0435*
[38] *University of Virginia, Charlottesville, Virginia 22901*
[39] *College of William and Mary, Williamsburg, Virginia 23187-8795*
[40] *Yerevan Physics Institute, 375036 Yerevan, Armenia*
(Dated: September 25, 2015)

Unpolarized and beam-polarized four-fold cross sections $\frac{d^4\sigma}{dQ^2 dx_B dt d\phi}$ for the $ep \rightarrow e'p'\gamma$ reaction were measured using the CLAS detector and the 5.75-GeV polarized electron beam of the Jefferson Lab accelerator, for 110 $(Q^2, x_B, t)$ bins over the widest phase space ever explored in the valence-quark region. Several models of Generalized Parton Distributions (GPDs) describe the data well at most of our kinematics. This increases our confidence that we understand the GPD $H$, expected to be the dominant contributor to these observables. Through a leading-twist extraction of Compton Form Factors, these results support the model predictions of a larger nucleon size at lower quark-momentum fraction $x_B$.

PACS numbers: 12.38.-t, 13.40.Gp, 13.60.Fz, 13.60.Hb, 14.20.Dh, 24.85.+p

The internal structure and dynamics of the proton, the nucleus of the most abundant chemical element in the visible universe, still remain a mystery in many respects, more than 40 years after the evidence for its quark and gluon substructure. How are the spatial and momentum distributions of the quarks and gluons (*i.e.*, the partons) correlated inside the nucleon? How do the partons contribute to the bulk properties of the proton (mass, spin, charge,...)? These are some fundamental questions at the intersection of nuclear and particle physics which are still to be resolved.

In order to tackle these essential issues, a large experimental program was launched worldwide at Jefferson Lab (JLab), COMPASS and HERA, facilities using multi-GeV electromagnetic probes, to study deeply virtual Compton scattering (DVCS). In the valence-quark region, this corresponds to Compton scattering at the quark level, with the incoming photon radiated from the lepton beam. As in the study of atomic or nuclear structure, the energy and angular distributions of the scattered photon reflect the distribution in momentum and/or space of the targets, which in our case are the quarks inside the proton. At JLab, electron beams are used and the reaction to study proton structure is $ep \rightarrow e'p'\gamma$. It was shown [1–5] that this process, at sufficiently large squared electron momentum transfer $Q^2 = -(e - e')^2$ and small squared proton momentum transfer $t = (p - p')^2$ (in terms of the electron and proton four-vectors), could be interpreted in the framework
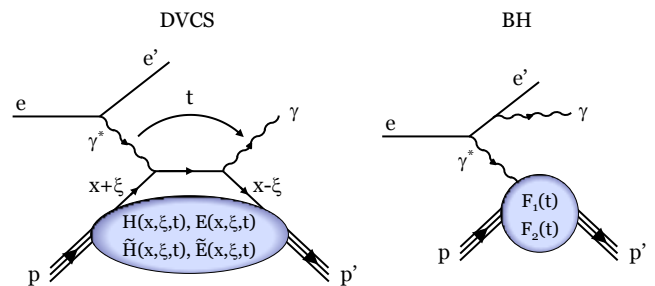
———
[*] corresponding author: jo@ipno.in2p3.fr
[†] Current address: Thomas Jefferson National Accelerator Facility, Newport News, Virginia 23606
[‡] Current address: Mississippi State University, Mississippi State, MS 39762
[§] Current address: Los Alamos National Laboratory, Los Alamos, NM 87544 USA
[¶] Current address: Old Dominion University, Norfolk, Virginia 23529

FIG. 1. Left: the dominant mechanism for the DVCS process at large $Q^2$ and small $|t|$, as predicted by the QCD factorization theorem. Right: the Bethe-Heitler (BH) process.

of Quantum Chromodynamics (QCD), the fundamental theory governing the interaction of quarks and gluons, as the product of the elementary Compton scattering at the quark level $\gamma^* q \rightarrow \gamma q$ with factorizable structure functions called Generalized Parton Distributions (GPDs).

Figure 1 (left) illustrates the GPD QCD factorization for the DVCS process. In a frame where the nucleon moves at the speed of light in a given direction, a quark with longitudinal momentum fraction $x + \xi$ along that direction absorbs the virtual photon and, after radiating the final-state photon, the *same* quark returns into the nucleon with a longitudinal momentum fraction $x - \xi$, plus some transverse kick included in $t$. The GPDs are functions of $x$, $\xi$, and $t$, and represent the probability amplitude of such a process. The variable $\xi$ is related to the Bjorken variable $x_B$: $\xi \approx \frac{x_B}{2 - x_B}$, where $x_B = \frac{Q^2}{2M\nu}$ with the proton mass $M$ and $\nu = E_e - E_{e'}$. Thus, it is determined by the scattered-electron kinematics. The quantity $x$ is not measurable in the DVCS process. At leading-order QCD, GPDs do not depend on $Q^2$. At leading-twist QCD (*i.e.*, when quark-gluon interactions and higher-order quark loops are neglected), four GPDs enter the description of the DVCS process: $H$, $\tilde{H}$, $E$ and $\tilde{E}$, representing the four independent helicity-spin tran-

sitions of the quark-nucleon system between the initial and final states. The GPDs are QCD matrix elements that project on a few variables the full complexity of the quarks' and gluons' dynamics within the nucleon.

The GPDs embody the longitudinal momentum distribution of the quarks in the nucleon, their transverse spatial distribution, and the correlation between these two distributions. One uses the term *nucleon tomography* as one can probe the transverse size of the nucleon for different quark longitudinal-momentum slices. For details on the GPD formalism, see the reviews [6–11].

In the $ep \to e'p'\gamma$ reaction, the DVCS process interferes with the well-known Bethe-Heitler (BH) process (Fig. 1, right), where the final-state photon is radiated by the incoming or scattered electron.

Extracting the GPDs from the DVCS process requires measuring a series of observables for the $ep \to e'p'\gamma$ reaction over the broadest kinematic domain possible. Several observables, such as the unpolarized cross section and polarized beam or/and target asymmetries, are necessary to separate the four GPDs. Each observable is sensitive to a particular combination of GPDs.

This article presents a major contribution to this global and long-term endeavour: the extraction of the $ep \to e'p'\gamma$ (*i.e.*, DVCS+BH) unpolarized and beam-polarized cross sections over the widest phase space ever explored in the valence-quark region, with 110 $(Q^2, x_B, t)$ bins covering: $1.0 < Q^2 < 4.6$ GeV$^2$, $0.10 < x_B < 0.58$, and $0.09 < -t < 0.52$ GeV$^2$. In this kinematic domain, our results strongly enhance the existing set of measurements of the $ep \to e'p'\gamma$ reaction which consists of: four $(Q^2, x_B, t)$ bins of unpolarized cross sections and 12 bins of beam-polarized cross sections measured by the JLab Hall A collaboration [12], 57 bins of beam-spin asymmetries [13] and 18 bins of longitudinal target- and beam-target double-spin asymmetries [14, 15] measured by the CLAS collaboration (in addition to the handful of CLAS pioneering data points from [16–18]).

The experiment took place at JLab during three months in 2005, using the 5.75-GeV polarized electron beam (79.4% polarization), a 2.5-cm-long liquid-hydrogen target, and the Hall B large-acceptance CLAS spectrometer [19], operating at a luminosity of $2\times10^{34}$ cm$^{-2}$s$^{-1}$. A specially designed electromagnetic calorimeter ("inner calorimeter", IC [13]) was added to the CLAS detector and allowed the detection of photons for polar angles from about $5°$ to $16°$, with full azimuthal coverage.

The first step of the data analysis was to select events with at least one electron, one proton, and one photon in the final state. Electrons were identified by signals in the CLAS drift chambers, scintillators, Cherenkov counters, and electromagnetic calorimeters. Protons were identified by the correlation between their measured momentum and velocity. The highest-energy particle detected in the IC was considered as a photon candidate. Once
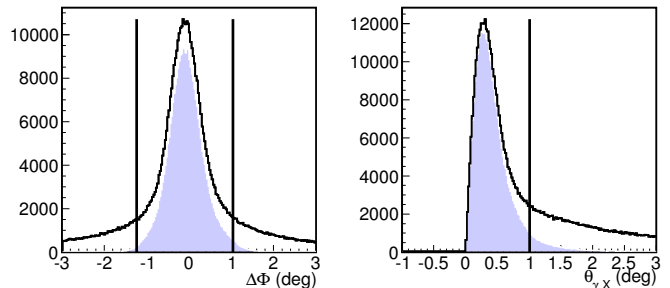


FIG. 2. (Color online) Two of the four variables on which $3\sigma$ exclusivity cuts (vertical lines) were applied to select the $ep \to e'p'\gamma$ reaction: $\Delta\phi$ and $\theta_{\gamma X}$. Black solid distributions show the events with at least one electron, one proton, and one photon, after applying the cuts on $MM^2_{e'p'}$. Each blue shaded distribution shows the events remaining after applying the cuts on all the variables except the plotted one.

these three final-state particles were selected and their 3-momenta determined, the exclusivity of the $ep \to e'p'\gamma$ reaction was ensured by applying $3\sigma$ cuts on the following four variables: the squared missing mass $MM^2_{e'p'}$ of the $(e'p'X)$ system, the coplanarity angle $\Delta\phi$, *i.e.*, the angle between the $(\gamma^*, p')$ and $(\gamma^*, \gamma)$ planes, the missing transverse momentum of the $(e'p'\gamma)$ system, and the angle $\theta_{\gamma X}$ between the measured photon and that predicted by the kinematics of the $(e'p'X)$ system. We also selected the particular kinematics: $W > 2$ GeV, where $W^2 = s = (\gamma^* + p)^2$, to minimize contributions from radiative decay of baryonic resonances, and $Q^2 > 1$ GeV$^2$ to be in the deep virtual regime. As an example, Fig. 2 shows the effect of two of the four exclusivity cuts.
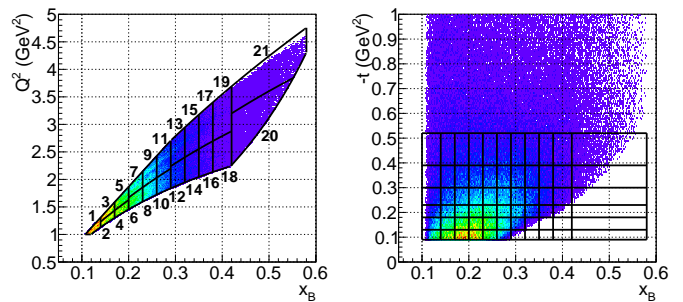


FIG. 3. (Color online) $(Q^2, x_B)$ and $(-t, x_B)$ kinematic coverages, with the corresponding binning.

Under these conditions, we ended up with about 300,000 events. Figure 3 shows the resulting $(Q^2, x_B)$ and $(-t, x_B)$ kinematic coverages of the data and the adopted binning [21 $(Q^2, x_B)$ bins and 6 $t$ bins], which is finer than the one used in [13]. Note that the bins and results presented here are limited to the $|t|$ region below $0.52$ GeV$^2$ while the actual coverage of the data goes beyond 1 GeV$^2$. The $ep \to e'p'\gamma$ cross sections vary very rapidly with kinematics, primarily due to the BH process. In order to minimize the uncertainties related to the knowledge of the kinematics, we minimized the size

of our bins, while keeping comparable statistics in each bin.

Due to the azimuthal symmetry when using an unpolarized target, the $ep \to e'p'\gamma$ reaction depends on four independent variables. For the study of GPDs, the most appropriate ones are $Q^2$, $x_B$, $t$ and $\phi$, where $\phi$ is the azimuthal angle between the $(e, e')$ and $(\gamma^*, p')$ planes around the virtual photon direction. We have thus extracted four-fold cross sections as follows:

$$\frac{d^4\sigma_{ep\to e'p'\gamma}}{dQ^2 dx_B dt d\phi} = \frac{N_{ep\to e'p'\gamma}}{\mathcal{L}_{int}\Delta Q^2 \Delta x_B \Delta t \Delta\phi \ Acc \ F_{rad}}. \quad (1)$$

In Eq. 1, $N_{ep\to e'p'\gamma}$ is the number of $ep \to e'p'\gamma$ events in the $(Q^2, x_B, t, \phi)$ bin. We evaluated the contamination from the $ep \to e'p'\pi^0$ channel where one photon of the $\pi^0$ decay can escape detection, using a combination of $ep \to e'p'\pi^0$ measurements and Monte-Carlo simulations. On average, this contamination is less than 9% and was subtracted on a bin-by-bin basis. The four-dimensional acceptance/efficiency of the CLAS detector, $Acc$, for the $ep \to e'p'\gamma$ reaction was determined for each $(Q^2, x_B, t, \phi)$ bin by generating more than 200 million DVCS+BH events, using a realistic Monte-Carlo generator adapted from [20]. The events were processed through the GEANT simulation of the CLAS detector, and the same reconstruction and analysis codes that were used for the data. The event generator includes radiative effects so that $Acc$ also corrects for a part of the real internal radiative effects. $F_{rad}$ corrects, for each $(Q^2, x_B, t, \phi)$ bin, for the virtual and the remainder of the real internal radiative effects, which can be both calculated theoretically [21]. The product $(\Delta Q^2 \Delta x_B \Delta t \Delta\phi)$ is the effective hypervolume of each bin. Finally, $\mathcal{L}_{int}$ is the integrated luminosity, corrected for the data acquisition dead time, which was deduced from the integrated charge of the beam measured by a Faraday cup. In addition, we applied a global renormalization factor of 12.3%, determined from the analysis of the elastic scattering $ep \to e'p'$, by comparing the experimental cross section to the well-known theoretical one. This factor compensates for various kinematic-independent inefficiencies, such as those from the CLAS time-of-flight scintillators and trigger, not well reproduced by the simulations.

Figure 4 shows, for two selected $(Q^2, x_B)$ bins in different parts of the phase space, the $\phi$-dependence of the $ep \to e'p'\gamma$ unpolarized cross section and beam-polarized cross-section difference. The latter of these two observables is defined as follows:

$$\Delta(d^4\sigma) = \frac{1}{2}\left[\frac{d^4\overrightarrow{\sigma}_{ep\to e'p'\gamma}}{dQ^2 dx_B dt d\phi} - \frac{d^4\overleftarrow{\sigma}_{ep\to e'p'\gamma}}{dQ^2 dx_B dt d\phi}\right], \quad (2)$$

where the arrows correspond to beam helicity states + and −. For each of these $(Q^2, x_B)$ bins, three selected $t$ bins are shown. Note that the data do not always provide a full coverage in $\phi$ for each of the 110 $(Q^2, x_B, t)$
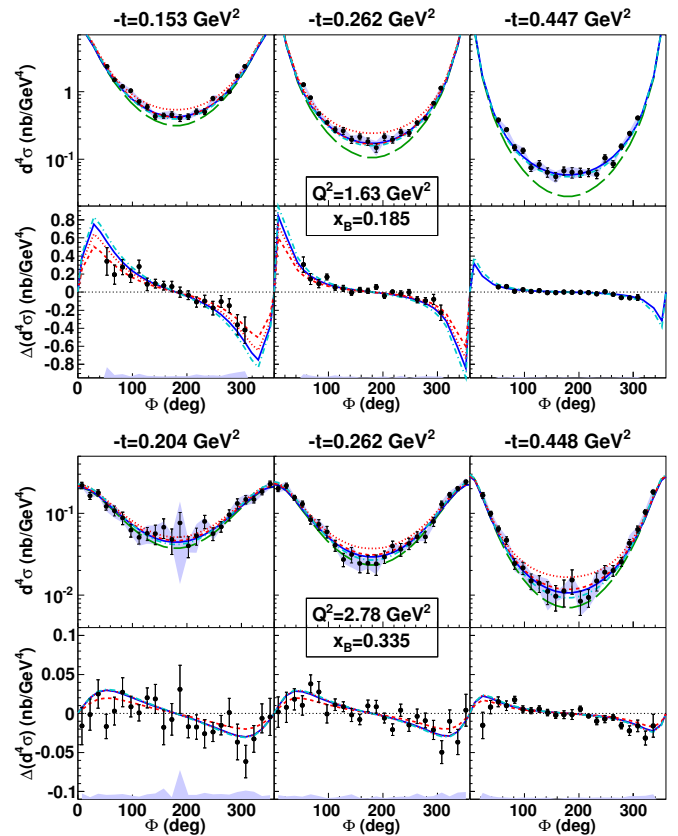


FIG. 4. (Color online) Top six plots: unpolarized cross section $\frac{d^4\sigma_{ep\to e'p'\gamma}}{dQ^2 dx_B dt d\phi}$ and beam-polarized cross-section difference $\Delta(d^4\sigma)$ for the $ep \to e'p'\gamma$ reaction, as a function of $\phi$, for $(Q^2, x_B)$=(1.63 GeV$^2$, 0.185) and three $-t$ values. Bottom six plots: same observables for $(Q^2, x_B)$=(2.78 GeV$^2$, 0.335) and three $-t$ values. The green long-dashed curves show the BH contribution only. The other curves are the predictions of four GPD models from three groups: VGG [6, 22, 23] (blue solid curves), KMS [24] (cyan dash-dotted curves), and two versions of the KM model [25, 26], KM10 (red dotted curves) and KM10a (red short-dashed curves). The blue bands show the systematic uncertainties.

bins. In Fig. 4, the black error bars show the statistical uncertainties of the data [13.9% on the unpolarized cross section on average, over the 110 $(Q^2, x_B, t)$ bins] and the blue bands show the systematic uncertainties [14% on the unpolarized cross section on average]. The contributions to the latter include the uncertainties on the beam energy and therefore the kinematics and associated corrections (5.7% on average, using a different beam energy value in the analysis), the acceptance correction (5.3%, with an alternate event generator), the global renormalization factor (5%), the exclusivity cuts (3.5%, from variations of the cuts), the radiative corrections (2.2%, including next-to-leading order effects), the particle selection (1.6%, from variations of the cuts), and the $\pi^0$ background subtraction (1%, with an alternate event generator).

The unpolarized cross sections peak towards $\phi=0°$ due to the BH process (green long-dashed curves in Fig. 4) for which the final-state photon is predominantly emitted in the direction of the initial or scattered electron. The difference between the BH curves and the data can thus be attributed to the DVCS process. We display in Fig. 4 calculations of four GPD models. The modeling of the GPDs in the VGG and KMS models is based on the Double-Distribution representation [1, 27, 28]. The VGG calculations in Fig. 4 only include the contribution of the GPD $H$ as the inclusion of the other GPDs barely changes the results. The KM model is based on the Mellin-Barnes representation [25, 29]. The KM10 version of the model includes contributions from all four GPDs for which the free parameters were fitted to the JLab [12, 13], HERMES [30] and ZEUS/H1 [31, 32] data. In that work, it was found that it is possible to fit the JLab Hall A unpolarized cross sections only at the price of introducing a very strong $\tilde{H}$ contribution [33]. The KM10a version is based on a fit which excludes the JLab Hall A unpolarized cross sections [12] and sets $\tilde{H}$ to zero. Note that none of these four models has been tuned to our data.

Figure 4 shows that the predictions of standard GPD models like VGG, KMS, and KM10a, whose compatibility is remarkable despite their different approaches, are in good agreement with our unpolarized cross-section data. In contrast, the KM10 version, which includes the strong $\tilde{H}$ contribution, tends to overestimate our data. Over our 110 $(Q^2, x_B, t)$ bins, the average $\chi^2$ value per degree of freedom [34] is the smallest for KM10a (1.46), followed by KMS (1.85), VGG (1.91), and KM10 (3.94). We can therefore conclude that standard GPD models with a dominant contribution of the GPD $H$ to the unpolarized cross section, *i.e.*, without the introduction of a strong $\tilde{H}$ contribution, describe the data well. Moreover, the disagreement between our data and the KM10 model, which instead matches the Hall A results, might reveal an inconsistency between the two sets of data. As a check, we performed a dedicated data analysis using the exact same $(Q^2, x_B, t)$ bin limits as those used for the Hall A analysis ($Q^2$=2.3 GeV$^2$, $x_B$=0.36, and $-t$ =0.17, 0.23, 0.28 and 0.33 GeV$^2$). However, in this limited and particular $(Q^2, x_B, t)$ region, the comparison is hampered by our large statistical uncertainties and lack of $\phi$-coverage around $\phi = 180°$. Thus no conclusion can be drawn from this comparison. The Hall A experiment was run at a luminosity almost three orders of magnitude larger than ours, but in a much more limited phase space.

Overall, the four models, including KM10, give a good description of the beam-polarized cross-section difference and the data barely allow one to distinguish one model from another. Over our 110 $(Q^2, x_B, t)$ bins, the average $\chi^2$ value per degree of freedom [34] is the smallest for KM10a (1.06), followed by KM10 (1.20), VGG (1.40), and KMS (1.84).
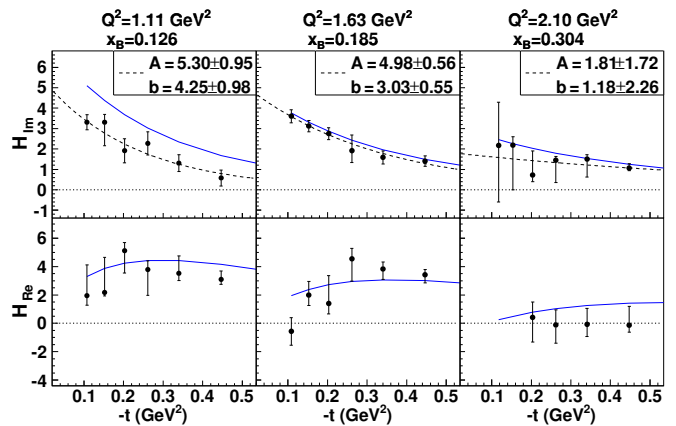


FIG. 5. (Color online) Results of the CFF fit of our data for $H_{Im}$ and $H_{Re}$, for three $(Q^2, x_B)$ bins, as a function of $t$. The blue solid curves are the VGG predictions. The black dashed curves show the fit of the results by the function $Ae^{bt}$.

Finally, we attempted to extract directly some GPD information from these two sets of observables. We used the local-fitting procedure developed in [35–38]. At leading twist and leading order, this procedure uses well-established DVCS and BH amplitudes, and fits simultaneously the $\phi$-distributions of our unpolarized and beam-polarized cross sections at a given $(Q^2, x_B, t)$ kinematic point by the (real) quantities:

$$F_{Re}(\xi, t) = \mathcal{P} \int_{-1}^{1} dx \left[ \frac{1}{x - \xi} \mp \frac{1}{x + \xi} \right] F(x, \xi, t),$$

$$F_{Im}(\xi, t) = F(\xi, \xi, t) \mp F(-\xi, \xi, t), \qquad (3)$$

where $F = H, \tilde{H}, E, \tilde{E}$, the top and bottom signs apply to the unpolarized $(H, E)$ and polarized $(\tilde{H}, \tilde{E})$ GPDs respectively, and $\mathcal{P}$ is the principal value integral. These quantities are called Compton Form Factors (CFFs) [39] in [35–38] and "sub-CFFs" in [40].

Here, we considered fits with only $H_{Im}$, $H_{Re}$, $\tilde{H}_{Im}$, and $\tilde{H}_{Re}$, which are the dominant CFFs, neglecting the contributions from $E$ and $\tilde{E}$. Despite the underconstrained nature of the problem, *i.e.*, fitting two observables with four free parameters, the algorithm generally manages to find, when the range of variation of the CFFs is limited, minimum $\chi^2$ values for $H_{Im}$ and $H_{Re}$ as the two fitted observables are dominated by the contribution of the GPD $H$. Figure 5 shows, for a selection of three of our 21 $(Q^2, x_B)$ bins, the $t$-distribution of the fitted $H_{Im}$ and $H_{Re}$. Contrary to these two, $\tilde{H}_{Im}$ and $\tilde{H}_{Re}$ do not come out of the fit with finite error bars within the allowed range of variation, for most kinematics. Nonetheless, they must be included in the fit because of their impact on the errors of $H_{Im}$ and $H_{Re}$. Figure 5 also shows the VGG predictions, which overestimates the fitted $H_{Im}$ at the smallest values of $x_B$.

We have fitted, in Fig. 5, the $t$-dependence of $H_{Im}$ by the function $Ae^{bt}$ with $A$ and $b$ as free parameters. Keeping in mind that the $Q^2$ values are different for the three

$x_B$ bins, the results of these fits show that $A$ and $b$ increase, in a systematic way, with decreasing $x_B$. Under the hypothesis of neglecting $Q^2$ higher-twist and evolution effects as well as *deskewing* effects [41], these behaviors might reveal tomographic features of the quark content of the nucleon. Under the mentioned conditions, $b$ is related to the transverse size of the nucleon. Our data therefore suggest that the size of the nucleon increases as lower momentum fractions (proportional to $x_B$) are probed. The rising of $A$ reflects the increase of the partonic content of the nucleon as lower $x_B$ values are probed. $H_{Re}$ does not lend itself easily to a simple interpretation as it involves a weighted integration of the GPD $H$ over $x$. Nevertheless, its extraction is of great use to constrain models.

In conclusion, we have measured the unpolarized and beam-polarized four-fold cross sections $\frac{d^4\sigma}{dQ^2 dx_B dt d\phi}$ for the $ep \to e'p'\gamma$ reaction over the widest phase space ever covered in the valence-quark region. The full data set, available at [42], will provide stringent constraints on GPD models. We have shown that three well-known GPD models describe the data well without additional inputs. The model interpretation of the present results favors a smaller deviation from the pure BH process around $\phi = 180°$ than suggested by the Hall A data. Within such models, this reinforces the expectation of the $H$-dominance in the unpolarized cross section. We have also extracted the $H_{Im}$ and $H_{Re}$ CFFs from our data. Under some assumptions, our results suggest that the nucleon size increases at lower parton-momentum values, thus revealing from experiment a first tomographic image of the nucleon.

[1] D. Mueller, D. Robaschik, B. Geyer, F.M. Dittes and J. Horejsi, Fortsch. Phys. **42**, 101 (1994).
[2] X.D. Ji, Phys. Rev. Lett. **78**, 610 (1997).
[3] X.D. Ji, Phys. Rev. D **55**, 7114 (1997).
[4] A.V. Radyushkin, Phys. Lett. B **380**, 417 (1996).
[5] A.V. Radyushkin, Phys. Rev. D **56**, 5524 (1997).
[6] K. Goeke, M.V. Polyakov and M. Vanderhaeghen, Prog. Part. Nucl. Phys. **47**, 401 (2001).
[7] M. Diehl, Phys. Rept. **388**, 41 (2003).
[8] X.D. Ji, Ann. Rev. Nucl. Part. Sci. **54**, 413 (2004).
[9] A.V. Belitsky and A.V. Radyushkin, Phys. Rept. **418**, 1 (2005).
[10] S. Boffi and B. Pasquini, Riv. Nuovo Cim. **30**, 387 (2007).
[11] M. Guidal, H. Moutarde and M. Vanderhaeghen, Rept. Prog. Phys. **76**, 066202 (2013).
[12] C. Muñoz Camacho *et al.* [Jefferson Lab Hall A Collaboration], Phys. Rev. Lett. **97**, 262002 (2006).
[13] F.X. Girod *et al.* [CLAS Collaboration], Phys. Rev. Lett. **100**, 162002 (2008). These beam-spin asymmetries were obtained with the same data set as in the present work.
[14] E. Seder *et al.* [CLAS Collaboration], Phys. Rev. Lett. **114**, 032001 (2015).
[15] S. Pisano *et al.* [CLAS Collaboration], Phys. Rev. D **91**, 052014 (2015).
[16] S. Stepanyan *et al.* [CLAS Collaboration], Phys. Rev. Lett. **87**, 182002 (2001).
[17] S. Chen *et al.* [CLAS Collaboration], Phys. Rev. Lett. **97**, 072002 (2006).
[18] G. Gavalian *et al.* [CLAS Collaboration], Phys. Rev. C **80**, 035206 (2009).
[19] B.A. Mecking *et al.*, Nucl. Instrum. Meth. A **503**, 513 (2003).
[20] I. Akushevich, H. Bottcher and D. Ryckbosch, Proceedings of the Hamburg 1998/1999 Workshop on Monte Carlo generators for HERA physics, 554-565 (1999).
[21] I. Akushevich and A. Ilyichev, Phys. Rev. D **85**, 053008 (2012).
[22] M. Vanderhaeghen, P.A.M. Guichon and M. Guidal, Phys. Rev. Lett. **80**, 5064 (1998); Phys. Rev. D **60**, 094017 (1999).
[23] M. Guidal, M.V. Polyakov, A.V. Radyushkin and M. Vanderhaeghen, Phys. Rev. D **72**, 054013 (2005).
[24] P. Kroll, H. Moutarde, and F. Sabatié, Eur. Phys. J. C **73**, 2278 (2013).
[25] K. Kumerički and D. Mueller, Nucl. Phys. B **841**, 1 (2010).
[26] K. Kumerički *et al.*, arXiv:1105.0899 [hep-ph].
[27] A.V. Radyushkin, Phys. Rev. D **59**, 014030 (1998).
[28] A.V. Radyushkin, Phys. Lett. B **449**, 81 (1999).
[29] D. Mueller and A. Schafer, Nucl. Phys. B **739**, 1 (2006).
[30] A. Airapetian *et al.* [HERMES Collaboration], Phys. Rev. Lett. **87**, 182001 (2001); JHEP **1207**, 032 (2012); JHEP **1006**, 019 (2010); JHEP **0806**, 066 (2008); Phys. Lett. B **704**, 15 (2011); Phys. Rev. D **75**, 011103 (2007); JHEP **0911**, 083 (2009); Phys. Rev. C **81**, 035202 (2010); JHEP **1210**, 042 (2012).
[31] S. Chekanov *et al.* [ZEUS Collaboration], Phys. Lett. B **573**, 46 (2003).

[32] A. Aktas *et al.* [H1 Collaboration], Eur. Phys. J. C **44**, 1 (2005).

[33] The introduced $\tilde{H}$ contribution is about a factor 3 larger than values given by standard parametrizations, such as in VGG, or inferred from simple relations to polarized Parton Distribution Functions.

[34] The $\chi^2$ values, integrated over all the bins, give a general indication but the level of agreement or disagreement between each GPD model's predictions and the data varies as a function of the kinematics.

[35] M. Guidal, Eur. Phys. J. A **37**, 319 (2008) [Erratum-ibid. A **40**, 119 (2009)].

[36] M. Guidal and H. Moutarde, Eur. Phys. J. A **42**, 71 (2009).

[37] M. Guidal, Phys. Lett. B **689**, 156 (2010).

[38] M. Guidal, Phys. Lett. B **693**, 17 (2010).

[39] The CFFs are alternatively defined as four complex quantities whose real and imaginary parts are respectively as: $\Re\mathcal{F}(\xi, t) = F_{Re}(\xi, t)$ and $\Im\mathrm{m}\mathcal{F}(\xi, t) = -\pi F_{Im}(\xi, t)$.

[40] K. Kumerički, D. Mueller and M. Murray, Nuovo Cim. C **036**, 159-165 (2013).

[41] The transition $H(\xi, \xi, t) \to H(\xi, 0, t)$ was estimated in a model-dependent fashion to be of the order of 20% in [11].

[42] CLAS Physics Database, `http://clasweb.jlab.org/physicsdb/`